ACS OMEGA

Open Access

http://pubs.acs.org/journal/acsodf

Article

Insights into the Dissociation Process and Binding Pattern of the BRCT7/8-PHF8 Complex

Longxiao Yuan, Xiaodan Liang,* and Lei He*

Cite This: *ACS Omega* 2024, 9, 20819−20831

Read Online

ACCESS | Metrics & More | Article Recommendations | Supporting Information

ABSTRACT: DNA topoisomerase 2-binding protein 1 (Topbp1) plays a crucial role in activating the ataxia-telangiectasia mutated and rad3-related (ATR) complex to initiate DNA damage repair responses. For this process to occur, it is necessary for PHF8 to dissociate from Topbp1. Topbp1 binds to the acidic patch sequence (APS) of PHF8 through its C-terminal BRCT7/8 domain, and disrupting this interaction could be a promising strategy for cancer treatment. To investigate the dissociation process and binding pattern of BRCT7/8-PHF8, we employed enhanced sampling techniques, such as steered molecular dynamics (SMD) simulations and accelerated molecular dynamics (aMD) simulations, along with self-organizing maps (SOM) and time-resolved force distribution analysis (TRFDA) methodologies. Our results demonstrate that the dissociation of PHF8 from BRCT7/8 starts from the N-terminus, leading to the unfolding of the N-terminal helix. Additionally, we identified critical residues that play a pivotal role in this dissociation process. These findings provide valuable insights into the disassociation of PHF8 from BRCT7/8, which could potentially guide the development of novel drugs targeting Topbp1 for cancer therapy.

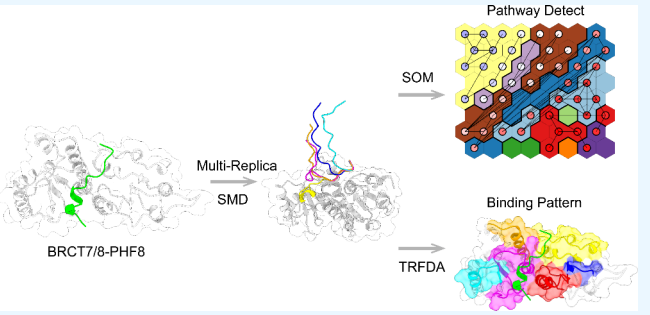

INTRODUCTION

The DNA damage response (DDR) is an evolutionary mechanism that organisms have developed over time through natural selection to counteract genetic damage factors, both internal and external.[1−3] Topbp1 plays a crucial role in the structure and function of DNA damage repair processes. On the one hand, it acts as a scaffold protein, bridging the ATR complex with the RAD9-HUS1-RAD1 (9−1−1) complex.[4−6] The ATR complex is involved in DNA damage repair, while the 9−1−1 complex is essential for activating ATR.[7,8] On the other hand, the C-terminus of Topbp1 contains the ATR activation domain (AAD), which is believed to activate ATR through allosteric regulation.[5,6] Topbp1 has nine highly conserved and repetitive BRCA1 C-terminal (BRCT) domains, starting from BRCT0 at the N-terminus.[9] Among these domains, the N-terminal BRCT0−2 can bind phosphorylated RAD9, inhibiting replication forks.[10] Recent research has also discovered that Topbp1 can reduce methylation levels by binding to plant homeodomain finger protein 8 (PHF8) through the C-terminal BRCT7/8.[11]

PHF8 is a histone demethylase that recognizes histone H3 lysine 4 (H3K4) methylation marks through its N-terminal PHD domain. Additionally, its C-terminal Jumonji C domain facilitates demethylation reactions of various lysine residues on histones.[12−14] The substrates of PHF8 are not only limited to histones.[15] The C-terminus of PHF8 contains an acidic patch sequence (APS) that can bind with the N-terminal BRCT7/8 of Topbp1. This binding leads to a reduction in the methylation levels of Topbp1.[11] Under physiological conditions, when single-stranded structures occur in the genome due to factors such as excised damaged double-stranded DNA or stalled replication forks, RAD17/RFC, a checkpoint clamp loader complex, initially localizes at the junction between ssDNA and dsDNA.[16,17] Subsequently, it triggers the recruitment of the 9−1−1 complex to this junction. At this stage, low-methylated Topbp1 is recruited and bound by RAD9.[11] Eventually, ATR binds to Topbp1, resulting in the formation of a complete complex and activation of ATR (Figure 1).[18,19]

Under physiological conditions, PHF8 undergoes phosphorylation and dissociates from Topbp1 in response to signals from cellular replication stress.[11] This allows Topbp1 to bind with RAD9, promoting the dissociation of Topbp1 from PHF8. This facilitates ATR activation and aids in genome repair. Studies indicate that unscheduled DNA damage response can result in harmful mutations, potentially leading to cell death or abnormal cellular behavior, such as cancer.[20,21] The development of small molecule inhibitors that disrupt the interaction between Topbp1 and PHF8 shows promise as a

Received: November 26, 2023
Revised: February 27, 2024
Accepted: April 24, 2024
Published: May 2, 2024

https://doi.org/10.1021/acsomega.3c09433
ACS Omega 2024, 9, 20819−20831

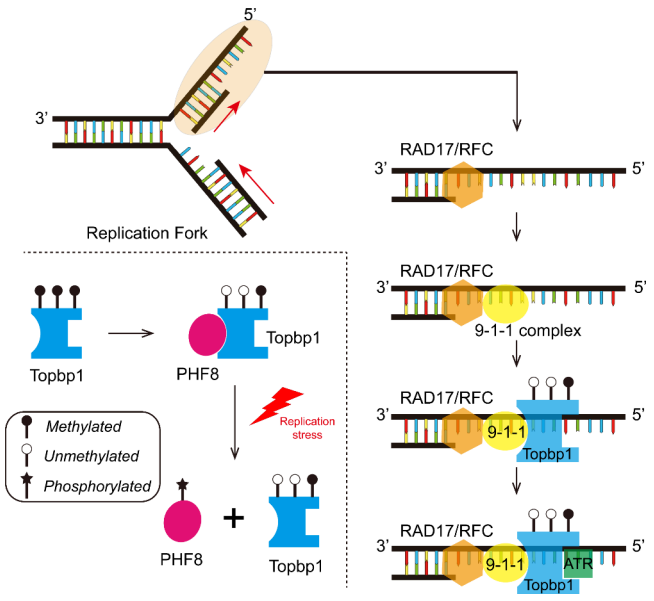

Figure 1. Bottom-left corner depicts the interaction relationship between Topbp1 and PHF8. The process of Topbp1's involvement in activating ATR is illustrated in the top-right corner, with red arrows indicating the direction of DNA synthesis.

new approach in cancer therapy. Fortunately, the structure of the Topbp1$^{BRCT7/8}$ and PHF8^{APS} complex has been resolved,[11] enabling structure-based drug design (Figure 2A). However, there is a scarcity of reports on this complex's dissociation process and binding pattern at the atomic level.

Molecular dynamics simulations are a reliable method for studying the microscopic movements of biomacromolecules. In this study, we utilized multireplica steered dynamics simulations, self-organizing maps (SOM),[22,23] and time-resolved force distribution analysis (TRFDA) to investigate the dissociation pathway of PHF8^{APS} and the critical residue pairs involved. Our findings indicate that PHF8^{APS} tends to dissociate starting from the N-terminus, accompanied by the unfolding of the N-terminal helix. Furthermore, several pairs of polar residues, primarily located in the F region of BRCT7/8 (residues 1462−1491) and the C-terminus of PHF8^{APS}, significantly resist PHF8^{APS} dissociation from BRCT7/8. These discoveries enhance our understanding of the PHF8^{APS} dissociation process and provide valuable insights for future research in drug design targeting Topbp1.

METHODS

Steered Molecular Dynamics (SMD) Simulations. The simulation was conducted using the GROMACS program (version 2021.4)[24] with the initial structure obtained from the protein data bank (PDB ID: 7CMZ,[11] crystal structure). Crystal water molecules and counterions were removed before the simulation. Missing residues in density were completed via homology modeling.[25] In the setup of the simulation system, the initial orientation of the complex was adjusted so that the interface between BRCT7/8 and PHF8^{APS} is parallel to the xy-plane. The AMBER FF14SB force field[26] was applied to the BRCT7/8-PHF8 system. If not specifically emphasized, the "PHF8" in "BRCT7/8-PHF8" in this article specifically refers to the APS motif of PHF8. Protonation states of residues in the complex were predicted using the Propka program.[27] The disulfide bond between C1299 and C844 is not present under physiological conditions and is not considered in this study.[11] The complex was placed in a rectangular explicit water box using the TIP3P water model and periodic boundary conditions. A distance of at least 10 Å was maintained between the edges of the box and any atom of the complex. Na^+ were added to maintain an overall neutral charge of the simulation system. Short-range nonbonded interactions were cut off at 1 nm, and long-range electrostatic interactions were treated using the Particle Mesh Ewald (PME) algorithm. The simulation system underwent 100 ps (50,000 steps with a time step of 2 fs) of constant-temperature (NVT, 298.15 K) equilibration, followed by another 100 ps (50,000 steps with a time step of 2 fs) of constant-pressure (NPT, 1 bar) equilibration.

After completing the equilibrium simulations, we initiated the dissociation of the BRCT7/8-PHF8 complex for the SMD simulations. This was achieved by applying a harmonic force on BRCT7/8 and PHF8^{APS}. To better understand the changes in interactions during the dissociation process and prevent system drift during pulling, BRCT7/8 was used as a fixed reference group. The distance between the center of mass of the two components was considered the dissociation coordinate. In the pulling simulation, PHF8^{APS} was pulled along the z-axis, away from BRCT7/8. It was pulled away from BRCT7/8 to 3.5−3.8 nm. We used a spring constant of 1000 kJ·mol^{-1}·nm^{-2} and a pulling rate of 0.1 nm·ns^{-1}.[28] We conducted 50 replicas of 26 ns SMD simulations, resulting in a total simulation time of 1.3 μs.

Self-Organizing Map Construction. The PathDetect-SOM package[29,30] was used to create the SOM matrix. Initially, the coordinates of Cα were extracted from each frame of the 50 SMD trajectories. These coordinates were used as input data for the PathDetect-SOM program. PHF8^{APS} was considered a ligand group. Before training, PathDetect-SOM used dRMSD values between BRCT7/8 and PHF8^{APS} as training features. The dRMSD calculation formula is shown below:[31]

$$\mathrm{dRMSD} = \sqrt{\frac{1}{N}\sum_{i=1}^{N}(r_i - r_i')^2} \quad (1)$$

In eq 1, N represents the number of atoms or particles in the structure, r_i and r'_i are the coordinates of corresponding atoms in two structures, and i denotes the index of the atom or particle. The training iterations were set to 5000 rounds, and to generate an 8 × 8 dimensional SOM matrix, the "dim" parameter was set to 8. Other parameters were kept at their default values.

Accelerated Molecular Dynamics (aMD) Simulations. The simulation was executed utilizing the Amber22 program.[32] Pre-equilibration was conducted under conditions of 298.15 K temperature and 1 bar pressure. Three parallel 500 ns simulation replicates were carried out, totaling a simulation duration of 1.5 μs. Specific parameter values were assigned in the input file for the production simulation: ethreshd = 13413.7, alphad = 1037.6, ethreshp = −601042, and alphap = 3349.6. The calculation formulas for these parameters are shown in eqs 2 − 5.[32]

$$\mathrm{ethreshp} = E_{\mathrm{potential}} + (0.16\ \mathrm{kcal\cdot mol^{-1}\cdot atom^{-1}} \times N_{\mathrm{atom}}) \quad (2)$$

$$\mathrm{alphap} = 0.16\ \mathrm{kcal\cdot mol^{-1}\cdot atom^{-1}} \times N_{\mathrm{atom}} \quad (3)$$

https://doi.org/10.1021/acsomega.3c09433
ACS Omega 2024, 9, 20819−20831

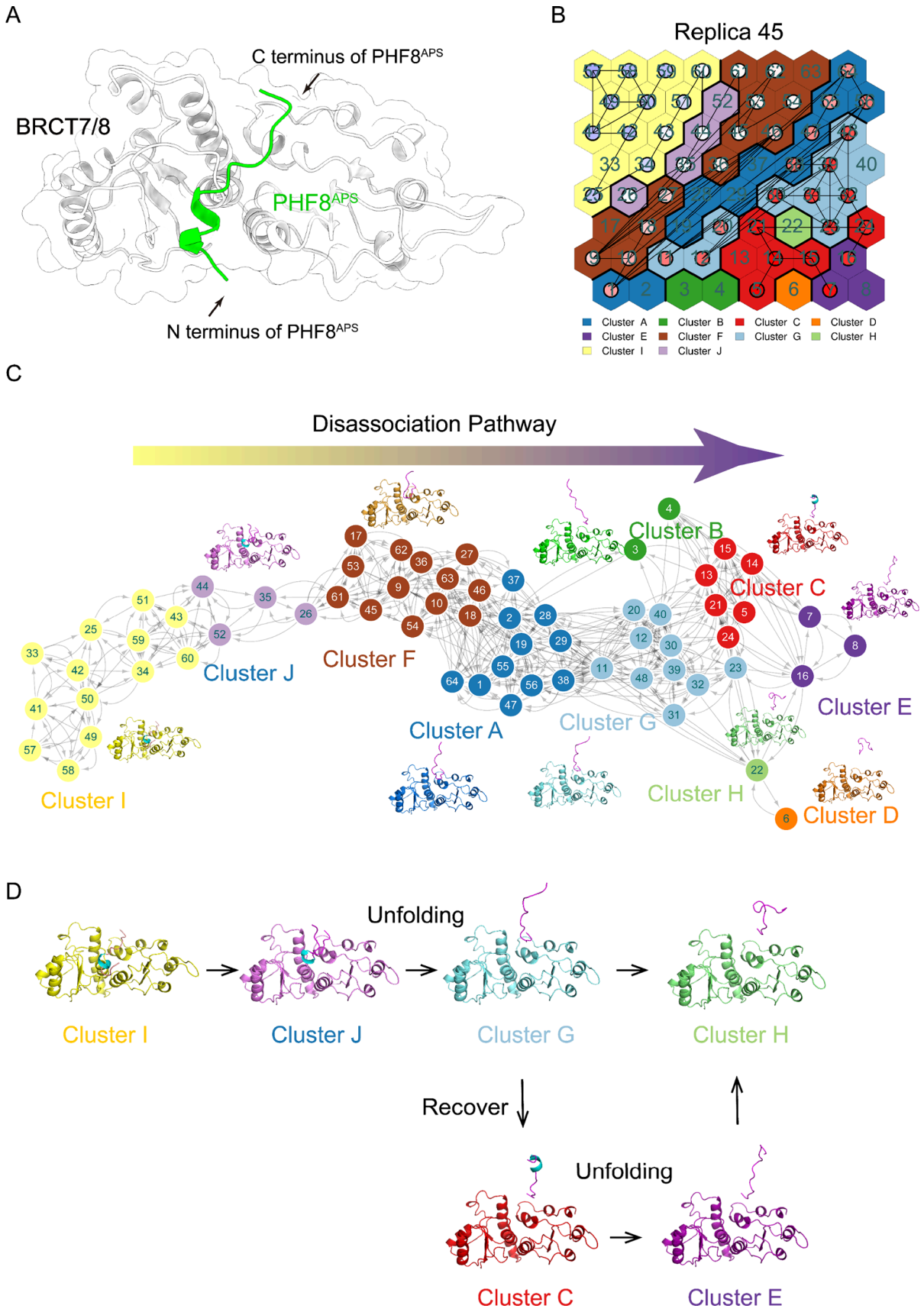

Figure 2. (A) The structure of the BRCT7/8-PHF8 complex. (B) The SOM matrix of Replica 45. (C) 64 neurons are organized in a transition network, with clusters highlighted in different colors and attached representative structures. BRCT7/8 and PHF8^{APS} share the same color scheme. PHF8^{APS} is color-coded based on secondary structure: α-helices are cyan, and disordered regions are magenta. (D) This diagram illustrates the separation of PHF8^{APS} from BRCT7/8.

https://doi.org/10.1021/acsomega.3c09433
ACS Omega 2024, 9, 20819−20831

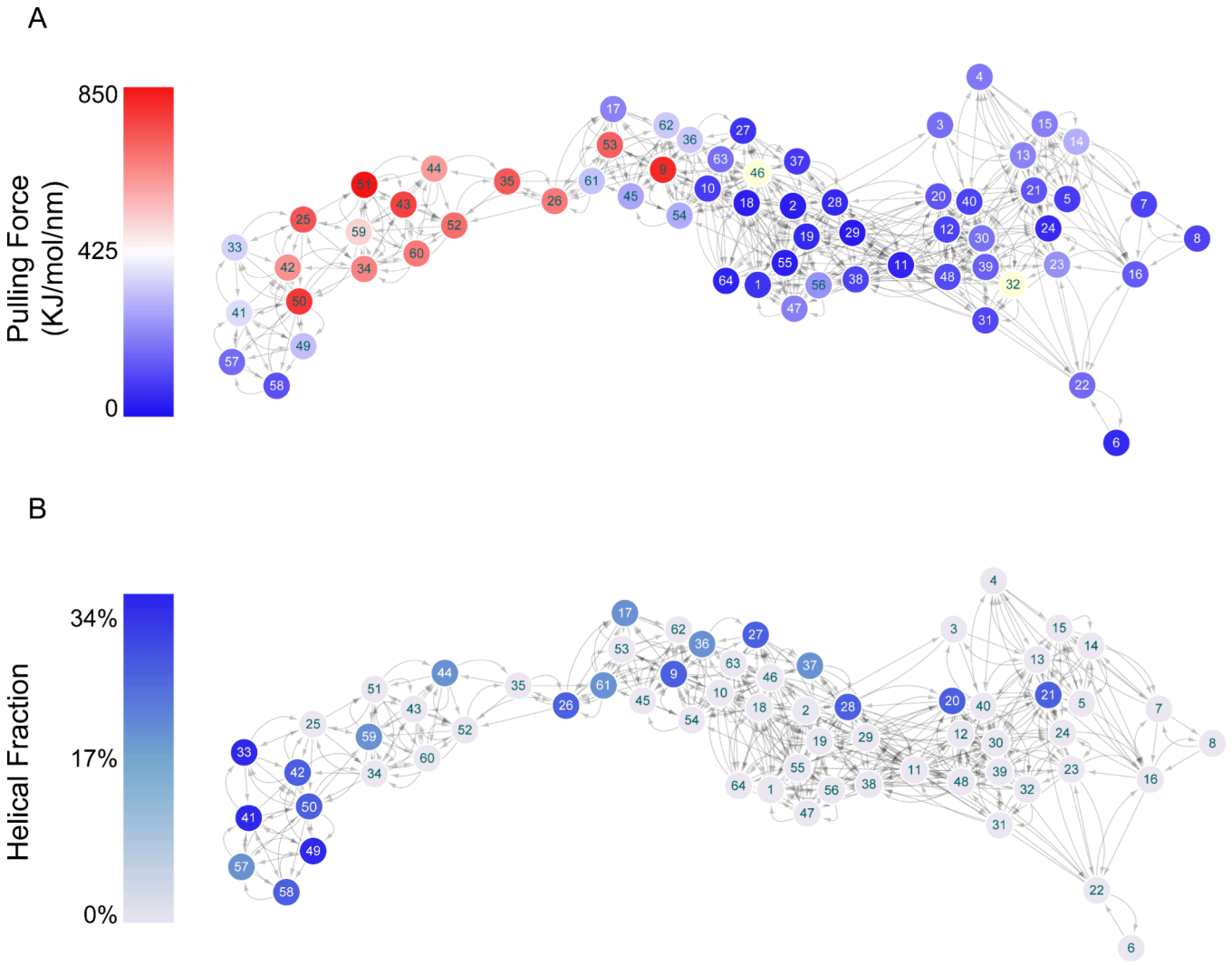

Figure 3. Pulling forces exerted on representative conformations (A) and the helical fractions of PHF8^{APS} (B) are mapped on the SOM. Neurons are labeled with their respective neuron indexes. In panel B, the helical fraction ranges from 0% to 100%, with 0% indicating the absence of a helical structure and 100% representing all residues forming a helical structure.

$$\text{ethreshd} = E_{\text{dihedral}} + (4\ \text{kcal·mol}^{-1}\text{·residue}^{-1} \times N_{\text{res}}) \quad (4)$$

$$\text{alphad} = \frac{1}{5} \times (4\ \text{kcal·mol}^{-1}\text{·residue}^{-1} \times N_{\text{res}}) \quad (5)$$

$E_{\text{potential}}$ and E_{dihedral} represent the average total potential energy and average dihedral energy of the complex system during the pre-equilibration experiments, measured in kcal·mol^{-1}. N_{atom} indicates the total number of atoms in the system, while N_{res} indicates the number of amino acid residues.

Umbrella Sampling. Multiple conformations were selected from the trajectory of Replica 45. For this study, 34 intermediate conformations were chosen as initial structures for separate 10 ns equilibrium samplings, resulting in a total simulation duration of 340 ns. The WHAM program, a module from Gromacs software, was utilized to plot the Potential Mean Force (PMF) against the pulling distance.

General Analysis of Simulation Trajectories. During the analysis of simulation trajectories, we computed several parameters such as RMSD (Root Mean Square Deviation), RMSF (Root Mean Square Fluctuation), SASA (Solvent Accessible Surface Area), distances, and changes in secondary structure over time. To conduct these analyses, we used the *cpptraj* module, which is a part of the AmberTools22 toolkit.

Time-Resolved Force Distribution Analysis. TRFDA aims to track the variations in atomic-level interaction forces for the targeted atoms/residues caused by a disturbance, such as the ligand binding/unbinding simulations. It calculates the sum of the absolute values of scalar pairwise forces acting on atom i:[33]

$$S_i = \sum_j |F_{ji}| \quad (6)$$

eq 6 defines stress, specifically referred to as punctual stress. This metric assesses the development of punctual stresses on individual residues within the SMD simulations. To determine the punctual stresses between the residues of PHF8^{APS} and BRCT7/8, TRFDA analysis was conducted on 50 replicas of SMD trajectories. Averaging was performed for each frame. The resulting punctual stresses were subsequently averaged over all SMD trajectories. Furthermore, a per-residue TRFDA analysis was performed on select crucial residues of PHF8^{APS} to investigate their interactions with BRCT7/8 and to track changes in these interactions throughout the simulations.

https://doi.org/10.1021/acsomega.3c09433
ACS Omega 2024, 9, 20819−20831

In Silico Mutation. The FoldX program[34] was utilized to predict the alterations in the Gibbs free energy of the BRCT7/8-PHF8 complex caused by mutations in essential residues to the remaining 19 natural amino acids. The cartoon structures were generated using ChimeraX[35] or Pymol,[36] and some figures were prepared using the Matplotlib package.

RESULTS

Dissociation Start at the N-Terminus of PHF8^{APS}. To gain a deeper understanding of the unbinding process of PHF8^{APS} and explore its mechanisms, we conducted 50 replicas of steered molecular dynamics (SMD). This extensive number of simulations was necessary to capture sufficient dissociation events involving the BRCT7/8-PHF8 complex. To identify a common dissociation pattern, we utilized self-organizing maps (SOMs), an unsupervised machine learning algorithm. This approach enabled us to represent these events in a lower-dimensional space, facilitating the identification of dissociation pathways.

For the training of the SOM model, we created an 8 × 8 neuron SOM by using the Cα atoms of BRCT7/8 and PHF8^{APS} that were extracted as input. The distances between these components in each frame were converted into a vector, allowing the program to iteratively modify the weights of the neurons. After 5000 training rounds, the model achieved convergence (Figure S1A). Subsequently, a collection of similar conformations was assigned to individual neurons, each representing a distinct conformation. Neurons exhibiting structural similarity were grouped into clusters. The 64 neurons were classified into 10 clusters (A−J) (Figure S2). As shown in Figure S1B, the distances between BRCT7/8 and PHF8^{APS} increased gradually from the top left to the bottom right. Mapping to Figure S2, Cluster I indicates a bonding state, whereas Clusters C, D, and E are closer to an unbinding state. To provide a clearer understanding, we extracted the representative conformations of each neuron and mapped them onto the SOM matrix, as illustrated in Figure S3.

Analyzing the transitions/pathways among 64 neurons across all 50 replicas, a consistent pattern was observed during the unbinding process. The process started from Cluster I (the native structure on the left), passed through Clusters J, F, A, and G (in the middle of the network), and ended at Cluster E/H/D (Figures 2B, S4). The transition network composed of neurons revealed that PHF8^{APS} consistently initiated dissociation from its N-terminus (Figure 2C). To provide a clearer representation, Figure 2D illustrates the disassociation pathway paradigm. Additionally, the representative structures of the top five clusters are superimposed, demonstrating a distinct progression of PHF8^{APS} dissociation from the N-terminus (Figure S5). It is worth noting that after Cluster G, the disassociation pathway diverged, leading to Cluster C and Cluster H. The representative conformation of Cluster C shows a helix that reemerges after Cluster J. (Figure 2D).

To investigate the correlation between the pulling force and the dissociation pathway, we measured the force exerted on each representative conformation of the neuron during the pulling process. These force values were then mapped onto the neuron network. The color gradient, ranging from blue to red, indicates the progressive increase in applied force (Figure 3A). Our findings indicate that the pulling force significantly increased at the onset of dissociation, with neurons 50, 51, 43, and 9 experiencing forces exceeding 800 kJ/mol/nm. This high force was sustained until the PHF8^{APS} N-terminal helix detached from BRCT7/8. Subsequently, the force gradually decreased. As the dissociation process advanced toward Cluster G, the force reached its minimum. However, during the dissociation process near Cluster C, there was an additional energy barrier needed to be overcome. This was evident from the force increase to approximately 425 kJ/mol/nm for neurons 14 and 23. This increase could be attributed to the hindrance caused by strong hydrogen bonding between the PHF8^{APS} C-terminal polar residues and BRCT7/8. This increase could be attributed to the hindrance caused by strong hydrogen bonding between the polar residues of the PHF8^{APS} C-terminal and BRCT7/8. In addition, we observed variations in the secondary structure of the PHF8^{APS} protein, particularly in the N-terminal helix, as it dissociated. We calculated the helical fraction of PHF8^{APS} in each representative conformation of the neuron and then mapped it onto the network. Based on our observations, it was found that during the dissociation process, the majority of neuron structures lost their helices. Following the dissociation of the N-terminal, only a small number of neuron structures (9, 20, 21, 27, and 28) retained the helix structure (Figure 3B). However, it is worth noting that these representative structures were not chosen as the representative conformations for their respective clusters, except neuron 21. This suggests that the scarcity of these conformations may have led to their exclusion from the contribution considered by the SOM.

Disassociation Process Was Accompanied by the Unfolding of the PHF8^{APS} α-Helix. The network previously constructed by SOM revealed that in most conformations assigned to neurons, the helix at the N-terminal of PHF8^{APS} unfolded after separating from the BRCT7/8 interface. However, a few neurons exhibited instances of a well-folded helix. To gain a deeper understanding of this phenomenon, we conducted a systematic analysis of the dynamic behavior of PHF8^{APS} across all replicas. To better distinguish detailed changes at the N-terminus during the dissociation process, the distance between the centroids of C1299$^{BRCT7/8}$ and G842^{PHF8} was initially measured (Figure 4A). We then monitored changes in this distance while considering parameters such as the number of hydrogen bonds between PHF8^{APS} and BRCT7/8, solvent-accessible surface area (SASA) of the N-terminal helical region of PHF8^{APS}, root-mean-square deviation (RMSD), and helical fraction.

In the analysis of SOM results, Replica 45 demonstrated a higher frequency of transitions among neurons and traversed a greater number of primary clusters compared to the other replicas. We conducted a statistical analysis on the number of neurons included in all 50 SMD replicas and observed that Replica 45 accounted for more than half of the neurons in all replicas (Figure S6A). This suggests that the conformation represented in Replica 45 is prevalent across multiple repeated SMD simulations, which eliminates potential random biases. Moreover, in the statistical analysis of the number of neurons experienced by each stretched replica, the majority of replicas included more than half of the total number of neurons. Additionally, several replicas (neurons 3, 6, 14, 28, 48) contained a similar number of neurons to Replica 45 (Figure S6B). Therefore, Replica 45 accurately reflects the general changes occurring in the BRCT7/8-PHF8 complex pulling process. Ultimately, we selected Replica 45 as the representative replica for subsequent analyses. Figure 4B demonstrates a noticeable rise in the distance between C1299$^{BRCT7/8}$ and G842^{PHF8} following the vertical line (line 1). At the same time,

https://doi.org/10.1021/acsomega.3c09433
ACS Omega 2024, 9, 20819−20831

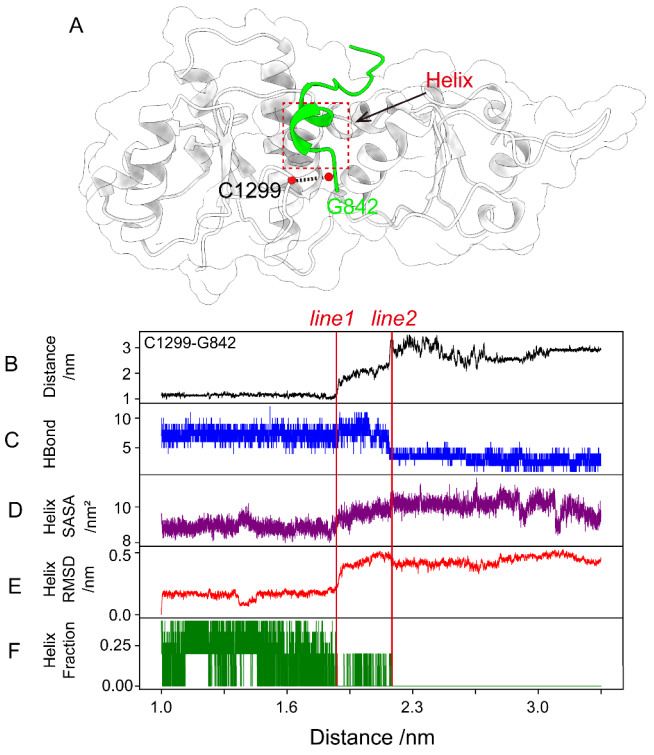

Figure 4. Disassociation process of the complex and the unfolding of the PHF8^{APS} α-helix, focusing on a representative disassociation pathway (replica 45). (A) The structure of the BRCT7/8 (white)−PHF8^{APS} (green) complex. The red circles denote residue centroids, while the dashed red frame outlines the helical region at the N-terminus of PHF8^{APS}. Panels B−F showcase various aspects of this pathway: (B) The distance between C1299$^{BRCT7/8}$−G842^{PHF8}. (C) The count of hydrogen bonds between BRCT7/8 and PHF8^{APS}. (D) The SASA of the PHF8^{APS} α-helix. (E) The RMSD of the PHF8^{APS} α-helix. (F) The helical fraction of PHF8^{APS}.

the SASA and RMSD of the N-terminal helix of PHF8^{APS} also exhibit an increase, suggesting the onset of PHF8^{APS} N-terminal dissociation. This pattern persists until reaching the position of the second vertical line (line 2), where the SASA and RMSD values stabilize. The number of hydrogen bonds between BRCT7/8 and PHF8^{APS} decreases significantly, suggesting a complete separation of the PHF8^{APS} N-terminus from BRCT7/8. During the transition from line 1 to line 2, the N-terminal helix of PHF8^{APS} undergoes a dynamic shift from complete to partial unfolding until it reaches complete unraveling, which persists after that without recovery (Figure 4C−F). To enhance reader comprehension, we have created an animation illustrating this process (SI_Movie.mp4).

In 46 out of 50 replicas, the PHF8^{APS} helix primarily unfolded after dissociation from BRCT7/8. However, the helix mostly remained intact in the remaining four replicas (38, 39, 44, and 47) (Figure S7). Nevertheless, even in these replicas, the helix underwent rapid transitions between unraveling and folding states. The pulling force reaches a minimum during the steered simulations between the first and second energy barriers. The N-terminal helix has a low probability of returning to its original folded conformation at low external forces. Throughout the dissociation of PHF8^{APS} from BRCT7/8, the N-terminal helix tends to predominantly unravel.

To validate our inference, we conducted three replicate accelerated molecular dynamics (aMD) simulations for the BRCT7/8-PHF8 complex. During a time scale of 500 ns, we observed substantial progress toward convergence in all trajectories (Figure S8A). Monitoring the root-mean-square fluctuations (RMSF) of each residue in PHF8^{APS} (Figure S8B) revealed significant fluctuations in both the N-terminal and C-terminal regions throughout the simulation. The N-terminus exhibited particularly pronounced fluctuations. The secondary structure analysis revealed that the N-terminal helix was not maintained in all trajectories (Figure S8, C−E). These findings support our previous inference and provide evidence for the dissociation process of PHF8^{APS} occurring simultaneously with the unfolding of the N-terminal helix.

To gain deeper insights into the dissociation of PHF8^{APS}, The SMD trajectory of Replica 45 was divided into 34 windows, and independent 10 ns equilibrium sampling was performed in each window (Figure S9A). This approach allowed us to generate a curve depicting the potential of mean force (PMF) of the PHF8^{APS} dissociation process against the pulling distance, providing new insights from an energy perspective. In Figure S9B, points ① and ② correspond to the positions of line 1 and line 2 in Figure 4, respectively. At position ①, there are two hydrogen bonds between G841^{PHF8} and S1406$^{BRCT7/8}$, which are disrupted as the pulling progresses. Simultaneously, there is partial disruption in the N-terminal helix of PHF8^{APS}. When the pulling process reaches position ②, only the interaction between D847^{PHF8} and R1407$^{BRCT7/8}$ remains in the N-terminal helix. Upon the disruption of this interaction, the N-terminal helix of PHF8^{APS} completely disappears. Therefore, the process between points ① and ② can be considered as the unfolding of the helix.

Overall, from the application of external force to the initiation of dissociation at the N-terminus of PHF8^{APS}, an energy expenditure of 21.4 kcal·mol^{-1} is required. The disassociation of the N-terminus accounts for 5.1 kcal·mol^{-1} of this energy, while an additional 9.2 kcal·mol^{-1} is needed for the dissociation of the C-terminus.

C-Terminus of PHF8^{APS} Confers Significant Resistance to Its Dissociation. TRFDA allows researchers to measure the punctual stress on specific residues and analyze how these residues respond to external disruptions. The TRFDA analysis was conducted between BRCT7/8 and PHF8^{APS} for each SMD trajectory to avoid favoring any specific trajectory. This approach enabled assessing how the punctual stress evolves on each residue.

The resistance experienced by all residues on BRCT7/8 during the pulling process was examined. The distribution of these residues is primarily concentrated in six areas labeled as Region A (residues 1271−1281), Region B (residues 1294−1324), Region C (residues 1362−1377), Region D (residues 1393−1422), Region E (residues 1436−1442), and Region F (residues 1462−1491) (Figure 5A-B). Among the regions studied, B, C, and F demonstrated resistance throughout the process of PHF8^{APS} dissociation, while regions A and D ceased their resistance midway. Radar charts were utilized to illustrate the average stress experienced by each region (Figure 5C). The findings revealed that Region F experienced the highest punctual stress, followed by Region B and D.

The average stress experienced by residues on PHF8^{APS} was assessed, revealing higher stress on the C-terminus than on the N-terminus (Figure 6A). We set an 800 kJ/mol/nm threshold based on the maximum pulling force values distribution range (Figure 3A). Only five residues, namely D847, Y852, and S854 - E856, exceeded this threshold (Figure 6B). Statistical analysis revealed that the resistance encountered by the N-terminal

https://doi.org/10.1021/acsomega.3c09433
ACS Omega 2024, 9, 20819−20831

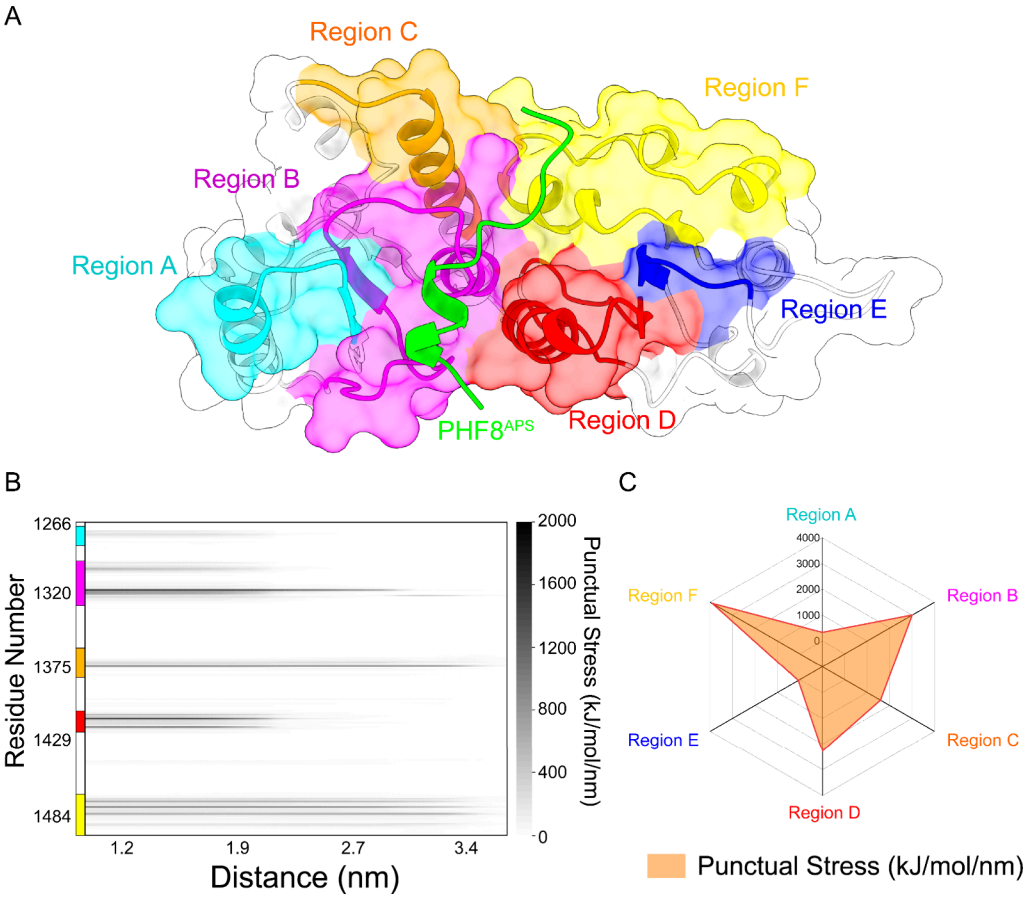

Figure 5. (A) Structure of BRCT7/8-PHF8 highlighting six defined regions in distinct colors. (B) Punctual stress on BRCT7/8 averaged over 50 SMD replicas. The color bar on the left corresponds to different regions on BRCT7/8. The horizontal axis represents the pulling distance. (C) Punctual stress on different regions of BRCT7/8 averaged over 50 SMD replicas.

residue D847 was significantly greater than that of the midsection residue Y852. Additionally, the resistance of Y852 was higher than that of the C-terminal residues S584, L855, and E856. These findings suggest that the maximum stress on $PHF8^{APS}$ is concentrated at the C-terminus, particularly with residues near the BRCT7/8 Region F. Additionally, based on our previous umbrella sampling results, it has been determined that the dissociation of the N-terminus contributes 5.1 kcal·mol^{-1} of energy, while an additional 9.2 kcal·mol^{-1} is required for the dissociation of the C-terminus. The N-terminus primarily consists of a helical secondary structure, and unwinding this structure necessitates energy. Therefore, it is probable that overcoming the dissociation resistance imposed by BRCT7/8 would require less than 5.1 kcal·mol^{-1}, which is significantly lower than the energy required for C-terminus dissociation. These findings indicate that the C-terminus of $PHF8^{APS}$ plays a more crucial role in its binding process with BRCT7/8.

The resistance of E856 during the dissociation process is significantly high. We conducted separate analyses of the residues within a 5 Å radius around $E856^{PHF8}$ in both the BRCT7/8-PHF8 crystal structure and the pre-equilibrium structure (Figure S10, A,B). In the crystal structure, $E856^{PHF8}$ is surrounded by several polar residues, but no hydrogen bond formation was detected. In the pre-equilibrium structure, we observed the absence of residue $M1474^{BRCT7/8}$ around $E856^{BRCT7/8}$, along with the presence of two additional polar residues, $E1476^{BRCT7/8}$ and $S1477^{BRCT7/8}$. Additionally, two strong hydrogen bond interactions were observed between $E856^{PHF8}$ and $R1369^{BRCT7/8}$. The number of hydrogen bonds formed between $E856^{PHF8}$ and surrounding residues was monitored during the stretching process of Replica 45 (Figure S10C). The hydrogen bonds formed with $E856^{PHF8}$ remained stable throughout the entire stretching process. Based on these findings, we conclude that the high punctual stress during dissociation of $E856^{PHF8}$ is mainly attributed to the abundance of polar residues surrounding it and the stable presence of strong hydrogen bond interactions.

Key Residues Involved in the Dissociation Process of BRCT7/8-PHF8. An analysis of the punctual stress experienced by $PHF8^{APS}$ during the dissociation process identified five key residues. These residues are D847 at the N-terminus, Y852 in the middle, and S854 to E856 at the C-terminus. In our discussion, we will refer to these three nonadjacent regions as I, II, and III, respectively (Figure 7A). Identifying the specific residue pairs involved in the dissociation process and analyzing their contributions along the pathway is crucial for better understanding the dissociation mechanism. To further investigate this, we focused on the five important residues of $PHF8^{APS}$ that are known to play a significant role in resisting dissociation. We performed per-residue TRFDA between each of these residues and BRCT7/8 to pinpoint the specific residue pairs that are essential for binding the BRCT7/8-PHF8 complex.

Figures 7E-G and S11 demonstrate that there are 14 essential pairwise interactions involved in the disassociation

https://doi.org/10.1021/acsomega.3c09433
ACS Omega 2024, 9, 20819−20831

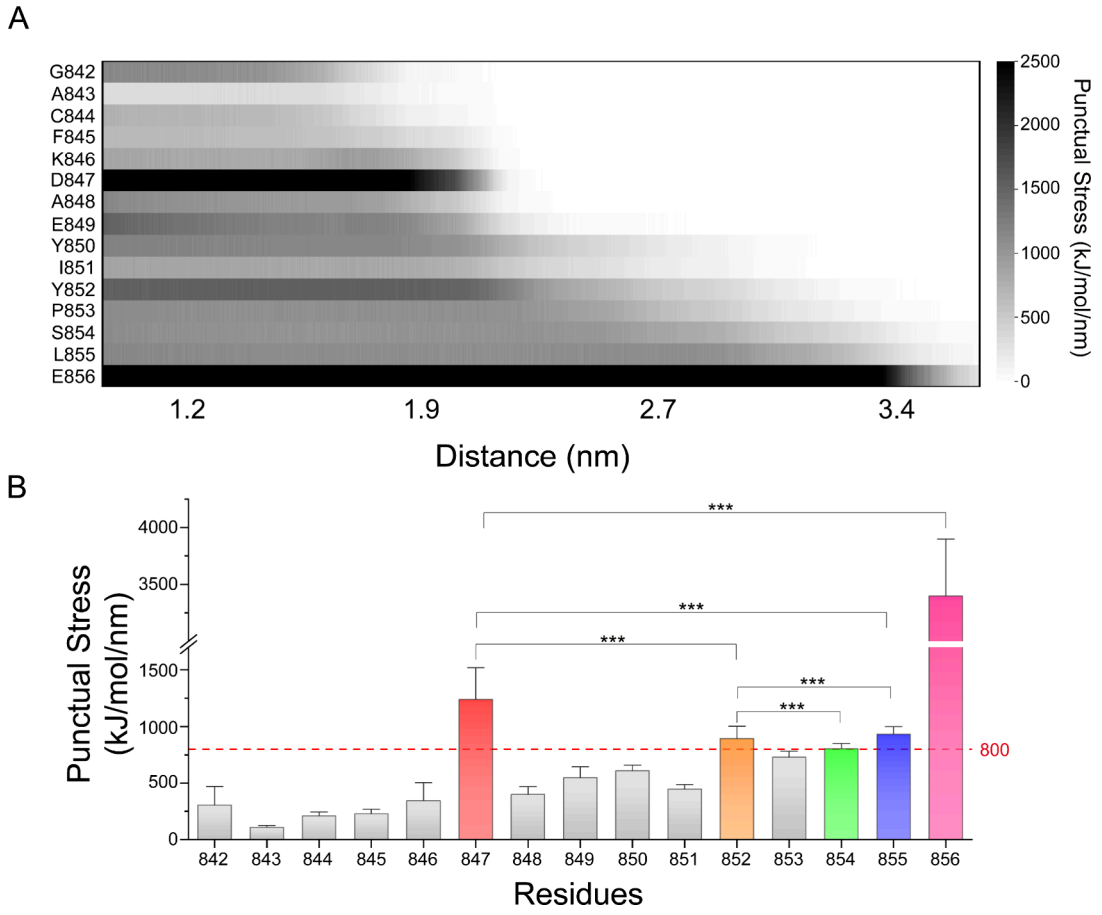

Figure 6. (A) Punctual stress on PHF8^{APS} averaged over 50 SMD replicas. The horizontal axis represents the pulling distance. (B) Punctual stress on each residue of PHF8^{APS} averaged over 50 SMD replicas. The red horizontal dashed line represents the 800 kJ/mol/nm reference line.

pathway. Including three pairs R1407/E1316/R1413$^{BRCT7/8}$-D847^{PHF8} in Region I; two pairs R1314/R1407$^{BRCT7/8}$-Y852^{PHF8} in Region II; nine pairs Y1318/R1369$^{BRCT7/8}$-E856^{PHF8}, D1471/Q1475/E1476$^{BRCT7/8}$-E856^{PHF8}, D1471/R1314$^{BRCT7/8}$-S854^{PHF8}, D1471/E1467$^{BRCT7/8}$ - L855^{PHF8} in Region III. The initial punctual stress exhibited by these key residue pairs was more significant than the interactions between PHF8^{APS} residues and the remaining BRCT7/8 residues. Analysis of the interaction types among these key residue pairs indicates that the interactions between BRCT7/8-PHF8 are predominantly polar−polar or positive−negative (Table S1). This emphasizes the critical role of polar interactions in the disassociation process.

To further narrow down the number of important residue pairs, we examined the correlation between the distance of residue pairs and the pulling distance. Our findings showed that in region I, the increase in distance for the D847^{PHF8}-R1407$^{BRCT7/8}$ pair was slightly slower compared to the D847^{PHF8}-E1316$^{BRCT7/8}$ and D847^{PHF8}-R1413$^{BRCT7/8}$ pairs (Figure 7H). This suggests that the hindrance effect of the D847^{PHF8}-R1407$^{BRCT7/8}$ pair is stronger during the dissociation process. Among the two residue pairs associated with Y852, Y852^{PHF8}-R1407$^{BRCT7/8}$ exhibited a stronger hindrance effect (Figure 7H). Among the five residue pairs associated with E856, the distance increment of E1476/Q1475$^{BRCT7/8}$-E856^{PHF8} noticeably lagged behind the other three pairs, indicating a stronger resistance to dissociation (Figure 7I). Similarly, we identified three key residue pairs: S854^{PHF8}-D1471$^{BRCT7/8}$, L855^{PHF8}-D1471$^{BRCT7/8}$, and L855^{PHF8}-E1467$^{BRCT7/8}$ (Figure S11, A−C). After thorough analysis, we have identified six key residue pairs through additional filtration. It is worth noting that R1407 and D1471 are present in two pairs of residues simultaneously, indicating their crucial role in stabilizing the BRCT7/8-PHF8 complex (Figure S12).

Validation of Key Residues. Six key residue pairs were identified in the dissociation process of BRCT7/8-PHF8 through TRFDA analysis. To validate this finding on the ten residues involved in these six key residue pairs, *in silico* mutations were performed on 19 other natural amino acids. The results indicated that mutations of R1407, D1471, E1467, Q1475, and E1476 on BRCT7/8 to other types generally increased the free energy, suggesting a decrease in overall structural stability (Figure 8A). This suggests that these residues have low substitutability and are highly conserved. However, there are a few exceptions. For instance, when D1471 was mutated to L, P, or M, it exhibited improved tolerance and enhanced system stability. This enhancement can be attributed to the proximity of D1471 to the hydrophobic residue L855 in PHF8^{APS}. After mutation, this residue contributed to system stability through hydrophobic interactions (Figure S13, A−D).

The *in silico* mutation results for the five key residues on PHF8^{APS} showed varying degrees of resistance to different types of mutations, especially within section III (Figure 8B). The polar residue D847 and aromatic residue Y852 demonstrated tolerance to mutations involving other polar

https://doi.org/10.1021/acsomega.3c09433
ACS Omega 2024, 9, 20819−20831

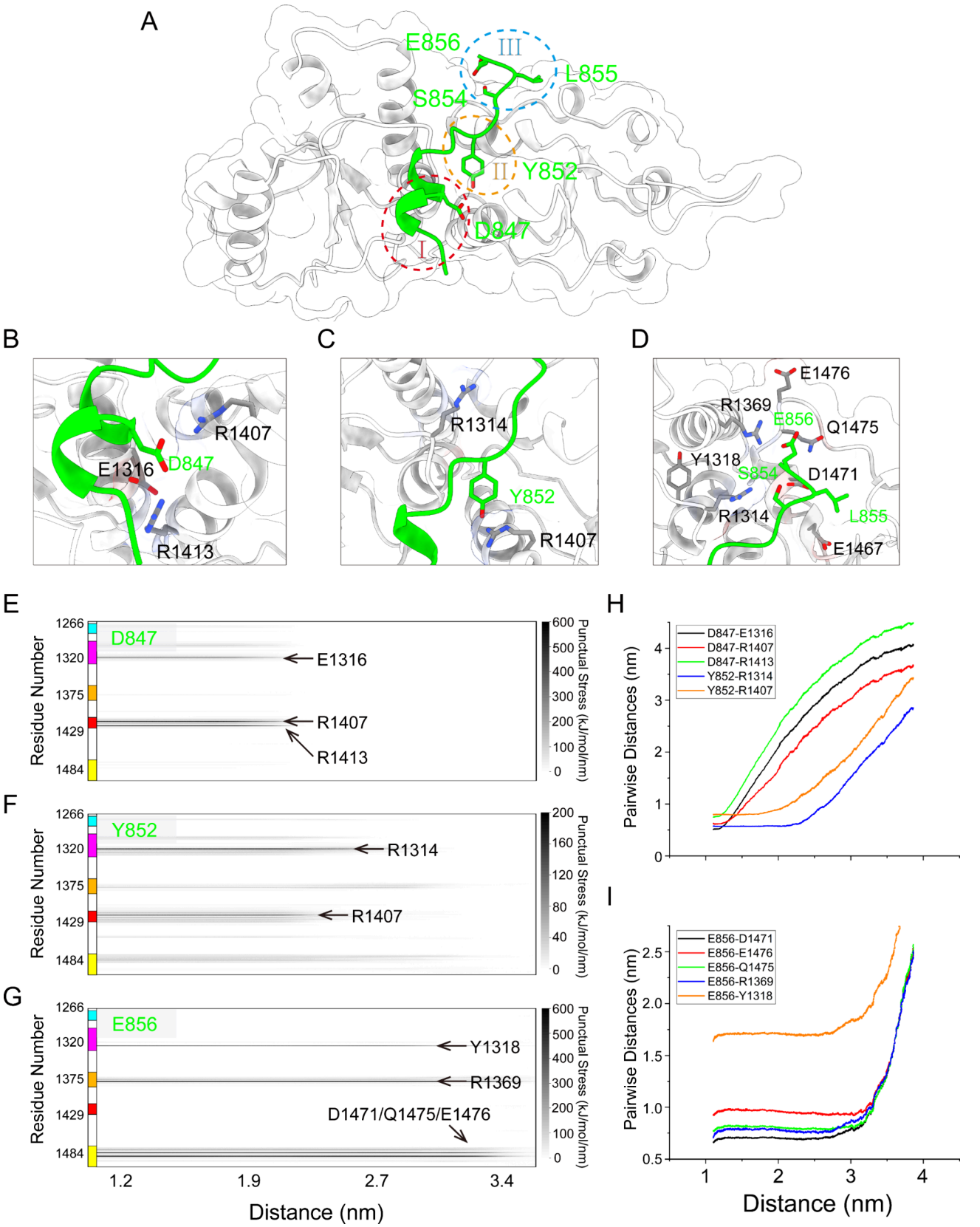

Figure 7. (A) The structure of BRCT7/8-PHF8, where dashed frames with different colors delineate PHF8^{APS} into three distinct regions (Regions I−III). (B−D) Detailed views of Region I−III. (E−G) Per-residue TRFDA between D847/Y852/E856 of PHF8^{APS} and BRCT7/8 in the dissociation pathway. (H, I) The corresponding pairwise distance changes along the dissociation process averaged over 50 SMD replicas.

and aromatic residues, respectively. Notably, D847 also exhibited higher tolerance to aromatic residues (W, Y, F), potentially due to its proximity to Y850 in PHF8^{APS}, which reduces the overall free energy through $\pi-\pi$ stacking

https://doi.org/10.1021/acsomega.3c09433
ACS Omega 2024, 9, 20819−20831

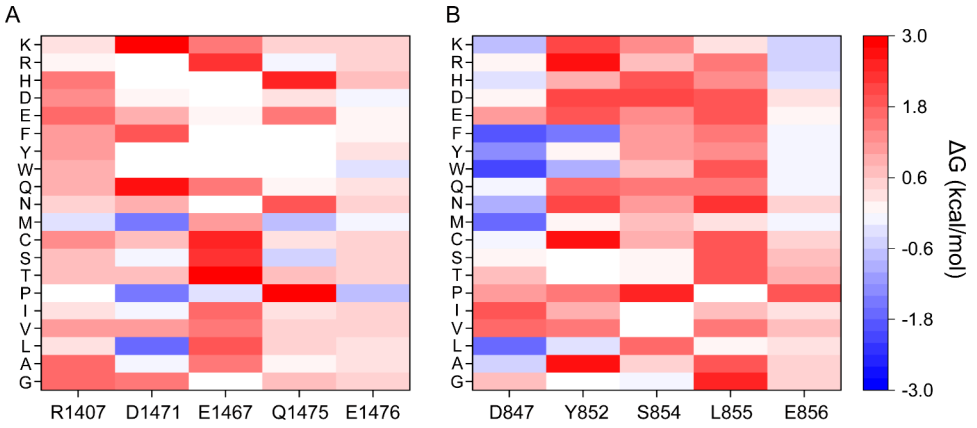

Figure 8. *In silico* mutation heatmap. (A) The heatmap matrix depicting mutations of key residues on BRCT7/8 to the other 19 natural amino acid residues. (B) The heatmap matrix illustrating mutations of key residues on PHF8^{APS} to the other 19 natural residues.

interactions (Figure S13, E−H). These six identified key residue pairs play a pivotal role in maintaining the BRCT7/8-PHF8 interaction. The results of *in silico* mutations provide additional support for our conclusions from another perspective.

DISCUSSION

In this study, we conducted SMD simulations with multiple replicas to expedite the dissociation of PHF8 from BRCT7/8. The simulation trajectories were subsequently analyzed using the Self-Organizing Map method. The analysis demonstrated that PHF8 dissociated from the N-terminus in all replicas. This dissociation process was accompanied by the dissociation of the N-terminal helix. However, these occurrences were infrequent enough to be overlooked by SOM. Furthermore, we observed the presence of two energy barriers that needed to be overcome during the dissociation process. The first barrier was encountered at the initial stage of N-terminal dissociation, while the second barrier emerged as PHF8 progressed toward the C-terminus. As the dissociation progressed into the midregion of PHF8 (Region II), the pulling force required reached a minimum (corresponding to cluster G in the SOM network). This decrease in pulling force reduced the impact on the N-terminal helix, which explains the presence of PHF8 helical structures in multiple conformations during this stage (e.g., neurons 9, 20, 27, 28).

To investigate the motion behavior of the BRCT7/8-PHF8 complex, we conducted three parallel 500 ns aMD simulations. Our results reveal substantial fluctuations in both the N-terminus and C-terminus of PHF8. Particularly, the fluctuations were more pronounced at the N-terminus, implying a greater likelihood for PHF8 to dissociate from this region. Furthermore, analysis of PHF8's secondary structure changes over time revealed instability in the N-terminal helical structure, further supporting our multireplica SMD observations.

To better understand the binding mode within the complex, we performed a TRFDA analysis on the dissociation process. The analysis showed that Region F of BRCT7/8 and Region III of PHF8 had the highest resistance to dissociation. We then identified 14 important residue pairs that played a significant role in resistance during dissociation. These residue pairs mainly exhibited polar−polar or positive−negative interactions. By analyzing the relationship between pairwise distance and pulling distance, we could narrow down to 6 key residue pairs. Among these key residues, two (R1407 and D1471) were present in multiple residue pairs simultaneously. Subsequently, *in silico* mutations were performed on these ten residues within the six key residue pairs. Each residue was mutated into 19 other natural amino acid residues separately. The results indicated that in most cases, when these residues were mutated, the system's free energy increased, suggesting instability. This finding highlights these residues' critical and irreplaceable roles in maintaining the BRCT7/8-PHF8 complex.

Shuai Ma et al. previously conducted a series of in vitro mutagenesis experiments on the BRCT7/8-PHF8 complex system to investigate the impact of specific residues on the binding behavior between BRCT7/8 and PHF8^{APS}.[11] They focused on mutating residues in three regions of BRCT7/8-PHF8 (Figure S14A). In Region I, D847 forms hydrogen bond interactions with R1413 and R1407 (Figure S14B). In our simulations, these two sets of hydrogen bonds persist throughout the first half of the dissociation process (SI_Movie.mp4). When D847 is mutated to A, the affinity between BRCT7/8 and PHF8^{APS} slightly decreases (approximately 3-fold reduction), and when R1413 is mutated to Q, they no longer bind. Based on the interactions observed among D847^{PHF8}, R1413$^{BRCT7/8}$, and R1407$^{BRCT7/8}$, as well as the results of the D847 mutation experiment, it can be concluded that simply disrupting the interaction between D847 and R1413 is not enough to fully terminate the interaction between BRCT7/8 and PHF8^{APS}. It has been hypothesized that the R1413Q mutation impacts the correct folding of BRCT7/8. In our study, D847 was also identified as a key residue during the PHF8^{APS} dissociation process. However, the mutation experiment results mentioned above imply that disrupting the physical interactions associated with D847 has limited efficacy in promoting PHF8^{APS} dissociation.

In Region II, Y852^{PHF8} is located near a shallow pocket, surrounded by hydrophobic residues such as F1411, L1414, I1469, and V1322 of BRCT7/8 (Figure S14C). This pocket consists mainly of hydrophobic properties, with two polar residues, R1407$^{BRCT7/8}$ and R1314$^{BRCT7/8}$, flanking the entrance. The binding of Y852 within the pocket is influenced by both its polarity and aromaticity, as evidenced by experimental data showing complete disruption of complex binding with Y852A and a 12-fold reduction in complex affinity with F1411A.[11] However, F1411A did not completely abolish the interaction between BRCT7/8 and PHF8^{APS}, indicating

https://doi.org/10.1021/acsomega.3c09433
ACS Omega 2024, 9, 20819−20831

that hydrophobic interactions in this region do not play a dominant role in their binding. Our study also highlights the significance of R1407 and R1314 in this region, suggesting that the polarity of Y852 primarily affects its binding. It is worth noting that Y850A also disrupts the interaction between BRCT7/8 and PHF8^{APS}. As Y850^{PHF8} is spatially close to Y852, it can influence the orientation of Y852 toward the benzene ring in the Y852 structure through $\pi-\pi$ stacking. Consequently, the removal of Y850 may lead to a misorientation of the Y852 side chain, potentially destabilizing the complex structure. In Region III, S854^{PHF8} forms hydrogen bond interactions with D1471$^{BRCT7/8}$ in the pre-equilibrated complex system (Figure S14D). Experimental results from mutations S854A and D1471A both indicate the disruption of the binding between PHF8^{APS} and BRCT7/8.

Overall, our study has identified that mutations in residues located in Region II and Region III, closer to the C-terminus of PHF8^{APS}, are more likely to disrupt the binding of PHF8^{APS} to BRCT7/8. Notably, key residues such as Y852, R1407, R1314, S854, and D1471 were identified in our experiments within these regions. The consistency between these findings and the outcomes of in vitro mutagenesis experiments suggests that Region II and Region III hold greater potential for drug development.[11] Conversely, Region I appears less favorable for drug development due to weaker binding strength of PHF8^{APS} observed in our simulation results and previous mutagenesis experiments. Moreover, Region I is in close proximity to the binding site of BACH1, which plays a crucial role in recruiting the ATR complex through Topbp1 to activate the DNA damage repair process (Figure S15A).[37] Targeting this region with drugs may hinder DNA damage repair by interfering with the binding of BACH1. In summary, Region I is not suitable for drug development. We have highlighted all the identified key residues on BRCT7/8, which are concentrated in Region II/III, particularly in Region III or F (Figure S15B). Inhibitors specifically designed to target this region, particularly those that can disrupt the interaction between the key residues in this region, have the potential to inhibit the binding of PHF8^{APS} to BRCT7/8 and promote PHF8^{APS} dissociation.

The full-length PHF8 protein consists of 1060 residues (Figure S16A).[38] Previous structural analyses have mainly focused on the PHD and Jumonji C domains, which are situated within the 1−500 residue range. However, only the structure of the APS motif, positioned beyond residue 500, has been experimentally determined.[11] AlphaFold2 predicts low confidence (pLDDT < 70) for residues 500 to 1060 primarily due to the absence of homologous templates for the entire C-terminal region of PHF8, suggesting high flexibility and challenging experimental resolution (Figure S16B).[39,40] Although PHF8 interacts with various proteins such as ARX, ICN1, and LSD1, the specific residues of PHF8 involved in these interactions are not yet fully elucidated.[41,42] If these proteins bind to the flexible C-terminal of PHF8, the impact on the secondary structure of PHF8^{APS} during its binding to BRCT7/8 or their dissociation behavior becomes unpredictable. While the F region of BRCT7/8 is identified as a potential druggable target in this study, further validation is necessary at the cellular level, considering the potential effects of full-length PHF8 and other interacting proteins.

CONCLUSION

This study utilized a combination of aMD, SMD, self-organizing maps, and time-resolved force distribution analysis to investigate the dissociation process between BRCT7/8 and PHF8^{APS}. Our findings indicate that PHF8^{APS} initiates dissociation from its N-terminus, accompanied by the unfolding of the N-terminal helix. Moreover, we have identified several critical residues that play essential roles in dissociation and validated their significance using FoldX. Additionally, we have observed significant resistance during dissociation at Region F of BRCT7/8 and Region III of PHF8^{APS}. These findings provide valuable insights into potential dissociation pathways of PHF8^{APS} and offer implications for drug development targeting BRCT7/8.

ASSOCIATED CONTENT

Supporting Information

The Supporting Information is available free of charge at https://pubs.acs.org/doi/10.1021/acsomega.3c09433.

Additional data, figures, and supplementary results (PDF)

Animation illustrating the process of the N-terminal helix of PHF8^{APS} undergoing a dynamic shift from complete to partial unfolding until it reaches complete unraveling (MP4)

AUTHOR INFORMATION

Corresponding Authors

Xiaodan Liang − *School of Computer Sciences and Technology, Tiangong University, Tianjin 300387, China*; Email: liangxiaodan@tiangong.edu.cn

Lei He − *Institute for Fetology, The First Affiliated Hospital of Soochow University, Suzhou 215006, China*; orcid.org/0009-0007-6381-0034; Email: lhe@suda.edu.cn

Author

Longxiao Yuan − *State Key Laboratory of Medicinal Chemical Biology, College of Pharmacy, Nankai University, Tianjin 300353, China*; orcid.org/0009-0002-5373-5783

Complete contact information is available at: https://pubs.acs.org/10.1021/acsomega.3c09433

Author Contributions

Lei He: Conceptualization, Supervision. Longxiao Yuan: Methodology, Visualization, Data curation, Writing - Original draft preparation. Xiaodan Liang: Provision of computational resources. Lei He and Longxiao Yuan: Writing - Review and Editing.

Funding

This work was financially supported by The Natural Science Foundation of the First Affiliated Hospital of Soochow University (BXQN2023024).

Notes

The authors declare no competing financial interest.

ACKNOWLEDGMENTS

We express our heartfelt appreciation to the Yang Lab at Nankai University, College of Pharmacy, for their invaluable inspiration. Their expertise and research contributions have significantly influenced the development of this research.

REFERENCES

(1) Scully, R.; Panday, A.; Elango, R.; Willis, N. A. DNA double-strand break repair-pathway choice in somatic mammalian cells. *Nature reviews Molecular cell biology*. **2019**, *20* (11), 698−714.

(2) Nasioudis, D.; George, E. M.; Xu, H.; Kim, H.; Simpkins, F. Combination DNA Damage Response (DDR) Inhibitors to Overcome Drug Resistance in Ovarian Cancer. In *Targeting the DNA Damage Response for Cancer Therapy*; Springer, 2023; pp 189−206.
(3) Malaquin, N.; Carrier-Leclerc, A.; Dessureault, M.; Rodier, F. DDR-mediated crosstalk between DNA-damaged cells and their microenvironment. *Frontiers in genetics.* **2015**, *6*, 94.
(4) Delacroix, S.; Wagner, J. M.; Kobayashi, M.; Yamamoto, K.-i.; Karnitz, L. M. The Rad9−Hus1−Rad1 (9−1−1) clamp activates checkpoint signaling via TopBP1. *Genes & development.* **2007**, *21* (12), 1472−1477.
(5) Mordes, D. A.; Glick, G. G.; Zhao, R.; Cortez, D. TopBP1 activates ATR through ATRIP and a PIKK regulatory domain. *Genes & development.* **2008**, *22* (11), 1478−1489.
(6) Kumagai, A.; Lee, J.; Yoo, H. Y.; Dunphy, W. G. TopBP1 activates the ATR-ATRIP complex. *Cell.* **2006**, *124* (5), 943−955.
(7) Blackford, A. N.; Jackson, S. P. ATM, ATR, and DNA-PK: The Trinity at the Heart of the DNA Damage Response. *Molecular cell.* **2017**, *66* (6), 801−817.
(8) Toledo, L. I.; Altmeyer, M.; Rask, M.-B.; Lukas, C.; Larsen, D. H.; Povlsen, L. K.; Bekker-Jensen, S.; Mailand, N.; Bartek, J.; Lukas, J. ATR prohibits replication catastrophe by preventing global exhaustion of RPA. *Cell.* **2013**, *155* (5), 1088−1103.
(9) Wardlaw, C. P.; Carr, A. M.; Oliver, A. W. TopBP1: A BRCT-scaffold protein functioning in multiple cellular pathways. *DNA repair.* **2014**, *22*, 165−174.
(10) Lee, J.; Kumagai, A.; Dunphy, W. G. The Rad9-Hus1-Rad1 checkpoint clamp regulates interaction of TopBP1 with ATR. *J. Biol. Chem.* **2007**, *282* (38), 28036−28044.
(11) Ma, S.; Cao, C.; Che, S.; Wang, Y.; Su, D.; Liu, S.; Gong, W.; Liu, L.; Sun, J.; Zhao, J.; et al. PHF8-promoted TOPBP1 demethylation drives ATR activation and preserves genome stability. *Science Advances.* **2021**, *7* (19), No. eabf7684.
(12) Liu, W.; Tanasa, B.; Tyurina, O. V.; Zhou, T. Y.; Gassmann, R.; Liu, W. T.; Ohgi, K. A.; Benner, C.; Garcia-Bassets, I.; Aggarwal, A. K.; et al. PHF8 mediates histone H4 lysine 20 demethylation events involved in cell cycle progression. *Nature.* **2010**, *466* (7305), 508−512.
(13) Qi, H. H.; Sarkissian, M.; Hu, G.-Q.; Wang, Z.; Bhattacharjee, A.; Gordon, D. B.; Gonzales, M.; Lan, F.; Ongusaha, P. P.; Huarte, M.; et al. Histone H4K20/H3K9 demethylase PHF8 regulates zebrafish brain and craniofacial development. *Nature.* **2010**, *466* (7305), 503−507.
(14) Iacobucci, S.; Padilla, N.; Gabrielli, M.; Navarro, C.; Lombardi, M.; Vicioso-Mantis, M.; Verderio, C.; de la Cruz, X.; Martínez-Balbás, M. A. The histone demethylase PHF8 regulates astrocyte differentiation and function. *Development.* **2021**, *148* (12), No. dev194951.
(15) Wu, Z.; Connolly, J.; Biggar, K. K. Beyond histones−the expanding roles of protein lysine methylation. *FEBS journal.* **2017**, *284* (17), 2732−2744.
(16) Yazinski, S. A.; Zou, L. Functions, regulation, and therapeutic implications of the ATR checkpoint pathway. *Annual review of genetics.* **2016**, *50*, 155−173.
(17) Zou, L.; Liu, D.; Elledge, S. J. Replication protein A-mediated recruitment and activation of Rad17 complexes. *Proceedings of the National Academy of Sciences.* **2003**, *100* (24), 13827−13832.
(18) Saldivar, J. C.; Cortez, D.; Cimprich, K. A. The essential kinase ATR: ensuring faithful duplication of a challenging genome. *Nature reviews Molecular cell biology.* **2017**, *18* (10), 622−636.
(19) Liu, S.; Shiotani, B.; Lahiri, M.; Maréchal, A.; Tse, A.; Leung, C. C. Y.; Glover, J. M.; Yang, X. H.; Zou, L. ATR autophosphorylation as a molecular switch for checkpoint activation. *Molecular cell.* **2011**, *43* (2), 192−202.
(20) Pilié, P. G.; Tang, C.; Mills, G. B.; Yap, T. A. State-of-the-art strategies for targeting the DNA damage response in cancer. *Nature reviews Clinical oncology.* **2019**, *16* (2), 81−104.
(21) Jackson, S. P.; Bartek, J. The DNA-damage response in human biology and disease. *Nature.* **2009**, *461* (7267), 1071−1078.
(22) Kohonen, T. The self-organizing map. *Proceedings of the IEEE* **1990**, *78* (9), 1464−1480.
(23) Kohonen, T. Essentials of the self-organizing map. *Neural networks.* **2013**, *37*, 52−65.
(24) Páll, S.; Abraham, M. J.; Kutzner, C.; Hess, B.; Lindahl, E. Tackling exascale software challenges in molecular dynamics simulations with GROMACS. In *Solving Software Challenges for Exascale: International Conference on Exascale Applications and Software, EASC 2014, Stockholm, Sweden, April 2−3, 2014*, Revised Selected Papers 2; Springer, 2015; pp 3−27.
(25) Webb, B.; Sali, A. Protein structure modeling with MODELLER. *Functional Genomics: Methods and Protocols.* **2017**, *1654*, 39−54.
(26) Maier, J. A.; Martinez, C.; Kasavajhala, K.; Wickstrom, L.; Hauser, K. E.; Simmerling, C. ff14SB: improving the accuracy of protein side chain and backbone parameters from ff99SB. *Journal of chemical theory and computation.* **2015**, *11* (8), 3696−3713.
(27) Jurrus, E.; Engel, D.; Star, K.; Monson, K.; Brandi, J.; Felberg, L. E.; Brookes, D. H.; Wilson, L.; Chen, J.; Liles, K.; et al. Improvements to the APBS biomolecular solvation software suite. *Protein Sci.* **2018**, *27* (1), 112−128.
(28) Li, T.; Motta, S.; Stevens, A. O.; Song, S.; Hendrix, E.; Pandini, A.; He, Y. Recognizing the Binding Pattern and Dissociation Pathways of the p300 Taz2-p53 TAD2 Complex. *JACS Au.* **2022**, *2* (8), 1935−1945.
(29) Motta, S.; Pandini, A.; Fornili, A.; Bonati, L. Reconstruction of ARNT PAS-B unfolding pathways by steered molecular dynamics and artificial neural networks. *Journal of Chemical Theory and Computation.* **2021**, *17* (4), 2080−2089.
(30) Motta, S.; Callea, L.; Bonati, L.; Pandini, A. PathDetect-SOM: A neural network approach for the identification of pathways in ligand binding simulations. *Journal of Chemical Theory and Computation.* **2022**, *18* (3), 1957−1968.
(31) Duarte, J. M.; Sathyapriya, R.; Stehr, H.; Filippis, I.; Lappe, M. Optimal contact definition for reconstruction of contact maps. *BMC bioinformatics.* **2010**, *11* (1), 1−10.
(32) Case, D.; Aktulga, H.; Belfon, K.; Ben-Shalom, I.; Berryman, J.; Brozell, S.; Cerutti, D.; Cheatham, T., III; Cisneros, G.; Cruzeiro, V. *AMBER 22*; University of California: San Francisco, CA, USA, 2022; pp 13−945.
(33) Costescu, B. I.; Gräter, F. Time-resolved force distribution analysis. *BMC biophysics.* **2013**, *6* (1), 1−5.
(34) Vanhee, P.; Verschueren, E.; Baeten, L.; Stricher, F.; Serrano, L.; Rousseau, F.; Schymkowitz, J. BriX: a database of protein building blocks for structural analysis, modeling and design. *Nucleic acids research.* **2011**, *39*, D435−D442.
(35) Goddard, T. D.; Huang, C. C.; Meng, E. C.; Pettersen, E. F.; Couch, G. S.; Morris, J. H.; Ferrin, T. E. UCSF ChimeraX: Meeting modern challenges in visualization and analysis. *Protein Sci.* **2018**, *27* (1), 14−25.
(36) DeLano, W. L. Pymol: An open-source molecular graphics tool. *CCP4 Newsl. Protein Crystallogr.* **2002**, *40* (1), 82−92.
(37) Leung, C. C.; Gong, Z.; Chen, J.; Glover, J. N. Molecular basis of BACH1/FANCJ recognition by TopBP1 in DNA replication checkpoint control. *J. Biol. Chem.* **2011**, *286* (6), 4292−4301.
(38) Kleine-Kohlbrecher, D.; Christensen, J.; Vandamme, J.; Abarrategui, I.; Bak, M.; Tommerup, N.; Shi, X.; Gozani, O.; Rappsilber, J.; Salcini, A. E.; et al. A functional link between the histone demethylase PHF8 and the transcription factor ZNF711 in X-linked mental retardation. *Mol. Cell* **2010**, *38* (2), 165−178.
(39) Jumper, J.; Evans, R.; Pritzel, A.; Green, T.; Figurnov, M.; Ronneberger, O.; Tunyasuvunakool, K.; Bates, R.; Žídek, A.; Potapenko, A.; et al. Highly accurate protein structure prediction with AlphaFold. *Nature* **2021**, *596* (7873), 583−589.
(40) Skolnick, J.; Gao, M.; Zhou, H.; Singh, S. AlphaFold 2: Why It Works and Its Implications for Understanding the Relationships of Protein Sequence, Structure, and Function. *J. Chem. Inf Model* **2021**, *61* (10), 4827−4831.

https://doi.org/10.1021/acsomega.3c09433
ACS Omega 2024, 9, 20819−20831

(41) Poeta, L.; Padula, A.; Lioi, M. B.; van Bokhoven, H.; Miano, M. G. Analysis of a Set of KDM5C Regulatory Genes Mutated in Neurodevelopmental Disorders Identifies Temporal Coexpression Brain Signatures. *Genes* **2021**, *12* (7), 1088.
(42) Yatim, A.; Benne, C.; Sobhian, B.; Laurent-Chabalier, S.; Deas, O.; Judde, J. G.; Lelievre, J. D.; Levy, Y.; Benkirane, M. NOTCH1 nuclear interactome reveals key regulators of its transcriptional activity and oncogenic function. *Mol. Cell* **2012**, *48* (3), 445−458.

https://doi.org/10.1021/acsomega.3c09433
ACS Omega 2024, 9, 20819−20831